Cyclic Blade Pitch Control Without a Swashplate

for Small Helicopters

James Paulos[a] and Mark Yim[b]
University of Pennsylvania, Philadelphia, PA 19104

This paper presents the design, dynamical model, and experimental investigation of an articulated rotor which affords cyclic pitch authority in small UAV rotorcraft without requiring either a mechanical swashplate or blade pitch actuators. An offset flap hinge coincident with a skew lag-pitch hinge is used to impose a positive lag-pitch coupling on one rotor blade and a complementary negative lag-pitch coupling on the other. The motor torque driving the propeller is electronically modulated to excite a lead-lag motion with controlled rotational phase and amplitude; the ensuing once-per-revolution variation in blade pitch obtains the conventional control response and flapping character of fully actuated cyclic systems. The governing nondimensional lag-flap equations including a non-constant speed hub are shown. The experimentally measured motor torque, the hub speed variation, the cyclic blade lag-pitch response, and the cyclic blade flapping response are compared to model predictions.

Nomenclature

a	section lift curve slope
A_β, A_ζ	flap and lag amplitude, rad
c	section chord length, m
c_{d_0}	section drag coefficient

[a] Ph.D. Candidate, Mechanical Engineering and Applied Mechanics, University of Pennsylvania, 220 South 33rd Street, Student Member AIAA.

[b] Professor, Mechanical Engineering and Applied Mechanics, University of Pennsylvania, 220 South 33rd Street.

c_β, c_ζ equivalent flap and lag hinge damping

c_m, k_m motor damping and stiffness coefficients

C_Q torque coefficient, $C_Q = Q/\rho\pi R^5\Omega^2$

dD, dL differential drag and lift forces, N

e offset hinge eccentricity

dF_y, dF_z differential section forces, N

G_D, G_P hinge geometry coefficients for disk and pin

i, i_0 motor current and no-load current, A

I_β flap inertia, $\mathrm{kg\,m^2}$

I_h hub inertia, $\mathrm{kg\,m^2}$

K_e motor emf constant, $\mathrm{V/(rad/s)}$ or $\mathrm{N\,m/A}$

K_I, K_P integral and proportional control gains

N_b number of blades

Q shaft torque, $\mathrm{N\,m}$

R blade tip radius, m

R_D, R_P hinge disk and pin radius, m

R_{ohm} motor electrical resistance, ohms

u additive modulation input

U_∞ incident velocity, m/s

U_P, U_T perpendicular and tangential incident velocity, m/s

v_i inflow velocity, m/s

V total motor terminal voltage, V

$\tilde{V}$ additive modulation voltage, V

X_{I_h} hub inertia ratio, $X_{I_h} = I_h/(N_b I_\beta)$

α angle of attack, rad

β flap angle, rad

γ Lock number, $\gamma = \rho a c R^4/I_\beta$

δ skew lag-pitch hinge angle, rad

ζ lag angle, rad

θ blade pitch, rad

$\Delta\theta/\Delta\zeta$ geometric lag-pitch coupling coefficient

μ_1 friction coefficient steel-plastic

μ_2 friction coefficient plastic-plastic

ξ spanwise blade station

ξ_1, ξ_2 axis rotation angles, rad

ρ air density, kg/m^3

σ rotor solidity, $\sigma = N_b c/(\pi R)$

ϕ inflow angle, rad, $\phi = U_P/U_T$

ϕ_i downwash angle, rad, $\phi_i = v_i/(\Omega R \xi)$

$\phi_{3/4}$ downwash angle at 3/4 spanwise station, rad

ψ hub orientation, rad

ω hub speed perturbation, $\omega = \dot{\psi} - \Omega$, rad/s

Ω hub speed average, rad/s

I.   Introduction

Obtaining the required attitude control authority for highly dynamic maneuvers and outdoor operation in small unmanned air vehicles (UAV) is a significant challenge in light of their stringent form factor and system weight requirements. Unlike the state of the art in conventional aircraft, miniature UAV platforms intended for photography, building inspection, and civilian security have largely converged on simple multi-rotor designs. While the mechanical simplicity of this approach is attractive, the need to accelerate and decelerate the rotor inertia to affect attitude corrections limits the available bandwidth of control. A much greater diversity of solutions is found in the research literature [1], motivated principally by the desire for ever smaller vehicles and higher control performance.

A number of different approaches have been proposed for borrowing aspects of conventional full scale helicopter controls and adapting them for small UAVs. Conventional helicopters are capable of rapidly changing their rotor pitch and generally do not rely on rotor speed changes for primary

thrust or attitude control as do multi-rotor aircraft. A simple example is collective pitch control, in which the blade pitch is uniformly increased or decreased to vary thrust. It has been been shown that adding collective pitch control to multi-rotor aircraft improves their flight capabilities and may be implemented with only a single actuator and relatively straightforward mechanical linkage system added for each rotor [2].

Another distinctive technology of conventional helicopters is cyclic control, which describes varying the blade pitch through each revolution of the rotor. This results in a cyclic variation in lift on each blade, a controlled blade flapping response, and ultimately useful control authority in pitch and roll derived from only a single rotor. Cyclic control in large aircraft is typically obtained by a linkage system which translates constant linear actuator setpoints in the non-rotating body frame into cyclic pitch variations in the rotating hub frame through the action of a mechanical swashplate. Several variations on this technique have been applied to small scale UAVs and have been investigated in the literature [3, 4]. These systems typically employ a swashplate mechanism that includes the swashplate bearing surface itself, several ball joint linkages, two or three ball servomotor actuators, and optionally a passive flybar system to augment passive damping or reduce the bandwidth requirements on the servomotor actuators. This direct mimicry of the large scale state of the art at miniature scale has proven effective; however the weight, size, assembly complexity, and requisite maintenance of these systems becomes significantly more burdensome as airframes grow exceptionally small.

Several programs have attempted to retain the benefits of cyclic control without the accompanying bulk of employing a full mechanical swashplate system. The muFly coaxial helicopter program proposed combining a simplified conventional swashplate with piezoelectric actuators instead of electromechanical servomotors [1, 5]. The Draper NAV program developed a tilting motor concept which again employed piezoelectric actuators but avoided the need for linkage rods in the rotating head itself [6]. In spite of these advances, integrating these control structures into actual flight vehicles remains a challenge.

The present work concerns obtaining a facsimile of conventional cyclic control without introducing auxiliary actuators of any kind. In this way a single rotor and motor can achieve thrust, roll,

and pitch authority. This preserves some of the advantages of cyclic control systems and avoids the multiplicity of rotors and supporting structures required by multi-rotor aircraft. At the same time, the mechanical simplicity of multi-rotor aircraft can be approached by eliminating the need for a swashplate system. The operating principle exploits the fact that the average rotor speed sets the thrust level, and so modulating the drive torque within each revolution presents an opportunity for additional axes of control. One early realization of this technique operated by inserting a torsional cantilever spring between the motor drive and the propeller itself [7]. Torque pulses delivered to the motor at specific stations in the rotation flexed the cantilever spring and directly twisted the blade along its feather axis. A later patent by Reich [8] describes conceptually how a hinged or flexible blade could respond directly to changes in torque with changes in blade pitch, but no mathematical model of the dynamics at work, simulation results, or experimental study were reported.

Most recently, experimental work by the authors explored a practical method for cyclic control which requires merely that the propeller be articulated with simple pin joints. Skewed lag hinges are employed to induce a positive lag-pitch coupling coefficient on one rotor blade and a negative lag-pitch coupling coefficient on the other. To establish a cyclic pitch response the motor torque is modulated in phase with the hub rotation; this induces a lead-lag response, cyclic variation in pitch, and useful control moments. Hub reaction forces and qualitative blade motions have been observed in test stand experiments [9]. In addition, the rotor has been incorporated into on a 227 g coaxial helicopter and flight experiments demonstrate trajectory tracking capabilities and in-flight power requirements [10]. These experimental successes affirm the basic conceptual principle for cyclic blade pitch control through torque modulation. However, in order to generalize this approach beyond the particular instances demonstrated in [9, 10] the need for a dynamical model with the ability to make quantitative predictions of cyclic blade motions must be addressed.

This paper presents design refinements, dynamical modeling, and quantitative experiments concerning the operation of an articulated propeller which couples modulated drive torques into cyclic pitch control. Section II reviews the operational concept and derives the modified blade kinematics which result from combining flap hinges with the skewed lag hinges employed previously. Section III develops the dynamical model governing the coupled lag-pitch-flap cyclic response which
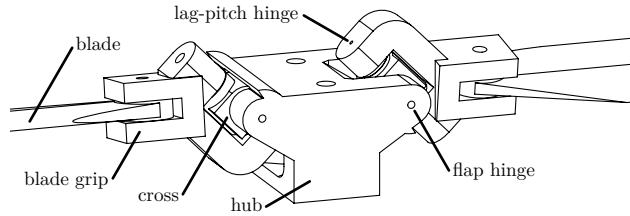
5

Fig. 1 The rotor hub with pin joints for flap hinges and skewed lag-pitch hinges.

allows the first quantitative analysis of the blade motions for this type of torque-driven cyclic system. Section IV describes the 32 cm diameter rotor prototype and drive electronics. Section V describes test stand experiments and provides a comparison of measured motor torque, hub speed, blade lag, and blade flap cyclic responses to model predictions. Closing remarks in Section VII discuss how this work might impact the design and performance of future small UAV systems.

II.   Design and Kinematics

The objective of the articulated rotor hub design is to allow modulating the drive shaft torque to induce controllable cyclic pitch variations. Our method is to kinematically induce a lag-pitch coupling through the combination of a conventional flap hinge and a skewed lag-pitch hinge. Figure 1 illustrates the physical device consisting of the hub, cross, blade grip, and blade bodies. The hub is attached to the cross by a flap hinge pin joint. The cross connects to the blade grip by a skewed lag hinge pin joint, and it is this skew angle that controls the degree of lag-pitch coupling. Similar hinge kinematics are depicted by Bousman [11] in the study of dynamic blade stability; now we exploit this structure as part of the control effector design. To this end the hub design is antisymmetric with a positive lag-pitch coupling imposed on one blade and a negative coupling imposed on the opposite blade. As a consequence, when a driving torque excites synchronous lead-lag motions in the two blades the pitch responses will be 180° out of phase with each other.

The addition of an explicit flap hinge is an improvement over previous work [9, 10] at the expense of a small addition in design complexity. It is apparent from Fig. 1 that in the absence of the flap hinge the blade tip on the right would be forced to flap down both as the blade leads forwards and lags backwards about the skewed axis. At the same time, the blade tip on the left would be forced to flap upwards twice per revolution as that blade obtains its maximum lead and lag angles.
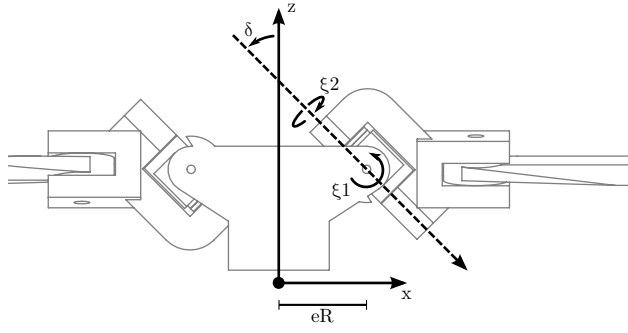
6

Fig. 2 Flap and skewed lag-pitch hinges are located coincident at radius eR**.**

The resulting flap motions for the two blades could not be matched, and these undesirable higher harmonics in the flapping response would contribute to large bending moments at the blade roots and unwanted airframe vibrations. The addition of a flap hinge relieves this kinematic constraint and allows the smooth sinusoidal flapping motion and conventional tip path plane response evident in the experiments.

The simplified kinematics are depicted in Fig. 2 with respect to a rotating hub-fixed coordinate system with unit vectors $\{\hat{\boldsymbol{x}}, \hat{\boldsymbol{y}}, \hat{\boldsymbol{z}}\}$. The kinematics and coordinate conventions for the positive lag-pitch coupling blade are shown on the right side of the figure. The hub rotates about the $\hat{\boldsymbol{z}}$ axis by angle ψ with respect to an inertial frame. The inboard flap hinge axis is fixed in the hub body and joins the cross body. The flap hinge rotates by an angle ξ_1 about an axis pointed in the $-\hat{\boldsymbol{y}}$ direction. The lag hinge axis of rotation is inclined by an angle δ from vertical to point in the $\sin(\delta)\hat{\boldsymbol{x}} - \cos(\delta)\hat{\boldsymbol{z}}$ direction, and the hinge rotates by an angle ξ_2. The flap hinge and lag hinge are collocated at radius eR for blade tip radius R and eccentricity $0 < e < 1$.

We would like to make a precise analogy between the actual kinematics of Fig. 2 and the conventional parameterization of blade motions in terms of orthogonal lag and flap axes. To do this, we consider small deflections of the blade about its physical hinges.

The composite rotation about first and second axes is conveniently described by exponential coordinates (or an axis and angle representation) when the rotations are infinitesimal. A finite rotation by angle ξ_1 about an axis with unit vector $\boldsymbol{\omega}_1$ is described by the rotation matrix $\exp(\hat{\boldsymbol{\omega}}_1 \xi_1)$ where $\hat{\boldsymbol{\omega}}_1$ is the skew symmetric matrix defined such that $\boldsymbol{\omega}_1 \times \boldsymbol{b} = \hat{\boldsymbol{\omega}}_1 \boldsymbol{b}$ for all $\boldsymbol{b}$. For the case of an infinitesimal rotation size $d\xi_1$, then to a first order approximation $\exp(\hat{\boldsymbol{\omega}}_1 \xi_1) = I + \hat{\boldsymbol{\omega}}_1 \, d\xi_1$. It
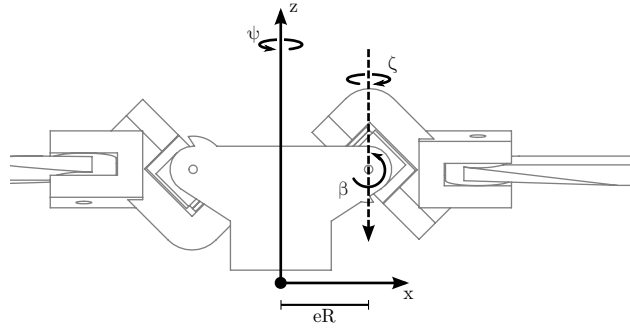
Fig. 3 Approximate kinematics with flap angle β, lag angle ζ, and imposed lag-pitch coupling.

follows that the composite rotation about axis $\boldsymbol{\omega}_1$ by angle $d\xi_1$ and then about axis $\boldsymbol{\omega}_2$ by angle $d\xi_2$ is $\exp(\hat{\boldsymbol{\omega}}_2 \, d\xi_2) \exp(\hat{\boldsymbol{\omega}}_1 \, d\xi_1) = I + (\boldsymbol{\omega}_1 \, d\xi_1 + \boldsymbol{\omega}_2 \, d\xi_2)^\wedge$ to a first order approximation. A physical interpretation of this result is simply that infinitesimal rotations commute, or that velocity vectors add. The exponential coordinates for the composite rotation dictated by the design geometry of Fig. 2 are expressed by

$$
\begin{bmatrix} 0 \\ -1 \\ 0 \end{bmatrix} d\xi_1 + \begin{bmatrix} \sin(\delta) \\ 0 \\ -\cos(\delta) \end{bmatrix} d\xi_2. \tag{1}
$$

For analysis, we re-parameterize the motion in terms of the canonical flap angle β about an axis in the $-\hat{\boldsymbol{y}}$ direction and lag angle ζ about the $-\hat{\boldsymbol{z}}$ direction, both axes fixed in the hub frame. This arrangement is shown in Fig. 3. We separately impose a geometric lag-pitch coupling coefficient $\Delta\theta/\Delta\zeta = \tan(\delta)$ and the resulting exponential coordinates for the composite rotation are

$$
\begin{bmatrix} 0 \\ -1 \\ 0 \end{bmatrix} d\beta + \begin{bmatrix} \Delta\theta/\Delta\zeta \\ 0 \\ -1 \end{bmatrix} d\zeta. \tag{2}
$$

The reparameterized expression encodes identical kinematics constraints as the original. The derived equation of motion, linearized for small deflections, will be equivalent if the flap and lag axes are coincident at eccentricity e and the rotational inertial of the small cross body and the blade about the pitch axis is neglected. This simplified parameterization in terms of the hub angle ψ, upward flap angle β, lag angle ζ, and geometric lag-pitch coupling coefficient $\Delta\theta/\Delta\zeta = \tan(\delta)$ will be used in the remainder.

III. Dynamical Model

The dynamical model consists of a linearized, nondimensional equation of motion for the propeller incorporating hub and blade inertial effects, aerodynamic forces, hinge losses, and the motor dynamics. This section considers each contribution in turn before constructing the final trim equation (Eq. 47) and perturbation equation (Eq. 50). A small number of torque-driven cyclic systems have been successfully tested based on a conceptual understanding of the operating principles [7, 9, 10]. However, the development and validation of an accurate dynamical model for this class of rotors is necessary in order to inform future experimental methods, rotor design and optimization, and vehicle integration efforts.

The usual treatment of rotor lag-flap dynamics is concerned with the question of stability and damping, and considers the hub speed to be a constant [11, 12]. In a departure from this view, we now consider modulation of the motor torque by an applied voltage as the critical input driving a blade pitch or blade flap response. As a result the model state must be expanded to include hub speed variations, and additionally the specifics of the motor dynamics and speed governor become relevant. Instead of explicitly modeling two blades, the analysis is simplified by taking advantage of approximate symmetry and modeling only one blade and appropriately normalizing the hub inertia and motor torques by the number of blades. The limitations of this conventional technique when applied to our not precisely symmetric blades are discussed with the experimental results.

A. Open-Chain Dynamics

The dynamics of the half propeller are developed as those of a three degree of freedom open-chain linkage with hub angle ψ, lag angle ζ, and flap angle β as defined in Fig. 3. The generic equation of motion is given by Eq. 3 where $\boldsymbol{q} = \{\psi, \zeta, \beta\}$, a general result for open-chain dynamical systems [13]. The inertial matrix $M(\boldsymbol{q})$ is a nonlinear function of the generalized coordinates and the Coriolis matrix $C(\boldsymbol{q}, \dot{\boldsymbol{q}})$ is a function of the coordinates and speeds. Both terms are derived directly from the kinematics depicted in Fig. 3 and inertial properties of the hub and blade body using the product of exponentials formula [13]. By convention, external (aerodynamic) forces applied to the rotor enter through $\boldsymbol{N}$ and joint torques from the motor and hinge losses enter on the right as

$\boldsymbol{\tau}_{motor}$ and $\boldsymbol{\tau}_{hinge}$.

$$M(\boldsymbol{q})\ddot{\boldsymbol{q}} + C(\boldsymbol{q},\dot{\boldsymbol{q}})\dot{\boldsymbol{q}} + \boldsymbol{N} = \frac{1}{N_b}\boldsymbol{\tau}_{motor} + \boldsymbol{\tau}_{hinge} \qquad (3)$$

In anticipation of deriving a linearized governing equation, we identify a steady trim condition at rotor speed Ω with coordinates $\boldsymbol{q}_0$ and velocities $\dot{\boldsymbol{q}}_0$ given by Eq. 4. Steady drag forces will cause the blades to lag backwards by a small positive angle ζ_0 and lift forces will cause the blades to flap upwards by a small positive coning angle β_0.

$$\boldsymbol{q}_0 = \{\Omega t, \zeta_0, \beta_0\}$$

$$\dot{\boldsymbol{q}}_0 = \{\Omega, 0, 0\} \qquad (4)$$

The linearized equation will be written in terms of perturbation variables $\boldsymbol{x}$, $\dot{\boldsymbol{x}}$ relative to this equilibrium.

$$\boldsymbol{x} = \boldsymbol{q} - \boldsymbol{q}_0 = \{\tilde{\psi}, \tilde{\zeta}, \tilde{\beta}\}$$

$$\dot{\boldsymbol{x}} = \dot{\boldsymbol{q}} - \dot{\boldsymbol{q}}_0 = \{\omega, \dot{\zeta}, \dot{\beta}\} \qquad (5)$$

The inertial acceleration term is approximated using a constant inertia matrix M found by evaluating the inertial matrix in the trim configuration. The Coriolis product is replaced by an affine approximation including an effective stiffness coefficient matrix K_C, an effective gyroscopic coefficient G_C, and an additive constant term $\boldsymbol{C_0}$. These terms are presented in Eq. 7-10. Their trigonometric dependence on the small constant trim lag and flap angles ζ_0 and β_0 have been approximated to first order by Taylor series expansion. For now the aerodynamic forces $\boldsymbol{N}$ and joint torques $\boldsymbol{\tau}_{motor}$, $\boldsymbol{\tau}_{hinge}$ are left as general functions and derived in the following sections.

$$M\ddot{\boldsymbol{x}} + G_C\dot{\boldsymbol{x}} + K_C\boldsymbol{x} + \boldsymbol{C_0} + \boldsymbol{N} = \frac{1}{N_b}\boldsymbol{\tau}_{motor} + \boldsymbol{\tau}_{hinge} \qquad (6)$$

$$M = I_\beta \begin{bmatrix} 1 + X_{I_h} + \frac{3e}{(1-e)^2} & -1 - \frac{3e}{2(1-e)} & 0 \\ -1 - \frac{3e}{2(1-e)} & 1 & 0 \\ 0 & 0 & 1 \end{bmatrix} \qquad (7)$$

10

$$K_C = I_\beta \Omega^2 \begin{bmatrix} 0 & 0 & 0 \\ 0 & \frac{3e}{2(1-e)} & 0 \\ 0 & 0 & 1 + \frac{3e}{2(1-e)} \end{bmatrix} \tag{8}$$

$$G_C = I_\beta \Omega \begin{bmatrix} 0 & -\frac{3e}{1-e}\zeta_0 & -(2+\frac{3e}{1-e})\beta_0 \\ \frac{3e}{1-e}\zeta_0 & 0 & 2\beta_0 \\ (2+\frac{3e}{1-e})\beta_0 & -2\beta_0 & 0 \end{bmatrix} \tag{9}$$

$$\boldsymbol{C}_0 = I_\beta \Omega^2 \begin{bmatrix} 0 \\ \frac{3e}{2(1-e)}\zeta_0 \\ \frac{2+e}{2(1-e)}\beta_0 \end{bmatrix} \tag{10}$$

In these expressions the flap inertia I_β defined in Eq. 11 assumes a total blade mass m evenly distributed between the hinge location at radius eR and the blade tip at radius R. The dimensionless hub inertia ratio X_{Ih} is the ratio of the hub inertia I_h to the flap inertia I_β and number of blades N_b.

$$I_\beta = \frac{1}{3}(1-e)^2 mR^2 \tag{11}$$

$$X_{I_h} = I_h/(I_\beta N_b) \tag{12}$$

B.   Aerodynamic Forces

The generalized aerodynamic forces about the hub axis, lag axis, and flap axis are required to establish the external forces $\boldsymbol{N}$ in Eq. 6. These moments are developed by integrating the local section forces along the blade length. The differential section forces F_z in the vertical direction and F_y in the chord direction are developed from section lift and drag forces L, D and a small angle approximation on the inflow angle ϕ.

$$dF_z = dL - \phi \, dD$$

$$dF_y = -\phi \, dL - dD \tag{13}$$

The local angle of attack $\alpha = \theta - \phi$ is the blade pitch angle θ less the local inflow angle ϕ. The inflow angle ϕ is determined from perpendicular and tangential local relative wind velocities U_P and U_T such that $\phi \simeq U_P/U_T$. The net incident wind speed U_∞ equates $U_\infty = \sqrt{U_P^2 + U_T^2}$. Lift and drag are determined from the section curve slope a and section drag coefficient c_{d_0}.

$$dL = \frac{\rho a c}{2} U_\infty^2 (\theta - \frac{U_P}{U_T}) \, dx$$

$$dD = \frac{\rho c}{2} U_\infty^2 c_{d_0} \, dx \tag{14}$$

The local velocities U_P and U_T are specialized for the case of a propeller with offset lag and flap hinges and hub with varying rotational speed $\dot\psi = \Omega + \omega$. Let v_i be the inflow velocity, $\Omega + \omega$ be the hub speed, β be the flap angle (positive up) and ζ be the lag angle (positive regressing). The local radius is ξR for tip radius R and nondimensional spanwise coordinate ξ with $0 \leq \xi \leq 1$, such that $dx = R \, d\xi$. The lag and flap hinges are located at a radius eR, offset from center by eccentricity e with $0 \leq e \leq 1$.

$$U_P = v_i + R(\xi - e)\dot\beta$$

$$U_T = R\xi(\Omega + \omega) - R(\xi - e)\dot\zeta \tag{15}$$

The section differential forces at blade station ξ are obtained from Eqs. 13–15 upon substitution. Higher order products of small terms ω, $\dot\zeta$, and $\dot\beta$ are neglected.

$$\begin{aligned}
dF_z = \frac{\rho a c \Omega^2 R^3}{2} \Bigg\{ &-(1 + \frac{c_{d_0}}{a})\xi \frac{v_i}{\Omega R} + \theta\left(\xi^2\right) \\
&+ \frac{\omega}{\Omega}\left(2\theta\xi^2 - (1 + \frac{c_{d_0}}{a})\xi \frac{v_i}{\Omega R}\right) \\
&- \frac{\dot\zeta}{\Omega}\left(2\theta\xi(\xi - e) - (1 + \frac{c_{d_0}}{a})(\xi - e)\frac{v_i}{\Omega R}\right) \\
&- \frac{\dot\beta}{\Omega}\left((1 + \frac{c_{d_0}}{a})\xi(\xi - e)\right) \Bigg\} d\xi
\end{aligned} \tag{16}$$

$$dF_y = -\frac{\rho a c \Omega^2 R^3}{2} \left\{ \frac{c_{d_0}}{a} \xi^2 - \frac{v_i^2}{\Omega^2 R^2} + \theta \left(\xi \frac{v_i}{\Omega R} \right) \right.$$

$$+ \frac{\omega}{\Omega} \left(2\frac{c_{d_0}}{a} \xi^2 + \theta \xi \frac{v_i}{\Omega R} \right)$$

$$- \frac{\dot{\zeta}}{\Omega} \left(2\frac{c_{d_0}}{a} \xi(\xi - e) + \theta(\xi - e) \frac{v_i}{\Omega R} \right)$$

$$\left. + \frac{\dot{\beta}}{\Omega} \left(\theta \xi(\xi - e) - 2(\xi - e) \frac{v_i}{\Omega R} \right) \right\} d\xi$$

(17)

The hub, lag hinge, and flap hinge moments are obtained by integrating the differential forces along the blade length, neglecting the effect of the blade root cutout as well as tip loss.

$$M_{\psi_{aero}} = R \int_0^1 \xi \, dF_y$$

$$M_{\zeta_{aero}} = -R \int_0^1 (\xi - e) \, dF_y$$

$$M_{\beta_{aero}} = R \int_0^1 (\xi - e) \, dF_z$$

(18)

In undertaking this integral, station weighted averages of the local downwash angle $\phi_i = v_i/(\Omega R \xi)$ and square of the downwash angle appear. In Eq. 19 we define parameters A and C as developed in [12] and new analogous parameters B, D, E which are anticipated by the extension to offset lag and flap hinges in [11].

$$A = 4 \int_0^1 \xi^3 \phi_i \, d\xi \qquad\qquad A_{3/4} = \phi_{3/4}$$

$$B = 4 \int_0^1 \xi^2 \phi_i \, d\xi \qquad\qquad B_{3/4} = \frac{4}{3} \phi_{3/4}$$

$$C = 4 \int_0^1 \xi^3 \phi_i^2 \, d\xi \qquad\qquad C_{3/4} = \phi_{3/4}^2$$

$$D = 4 \int_0^1 \xi^2 \phi_i^2 \, d\xi \qquad\qquad D_{3/4} = \frac{4}{3} \phi_{3/4}^2$$

$$E = 4 \int_0^1 \xi \phi_i \, d\xi \qquad\qquad E_{3/4} = 2\phi_{3/4}$$

(19)

The local downwash angle ϕ_i is determined from the local inflow velocity v_i, which may be calculated from blade element momentum theory within an annular ring at radius ξ. For the special case of a hovering rotor not in climb, Eq. 20 gives the inflow at blade station ξ as a function of solidity $\sigma = N_b c/(\pi R)$ [14].

$$\frac{v_i}{\Omega R} = \frac{a\sigma}{16} \left(\sqrt{1 + \frac{32\theta}{a\sigma} \xi} - 1 \right)$$

(20)

13

In the remainder of the derivation, these integrals are approximated by evaluating them assuming uniform downwash angle ϕ_i equal to the value at the three-quarters station radius, $\phi_{3/4}$. The expression for $\phi_{3/4}$ in Eq. 21 has been used previously in [12]. An advantage of expressing the results in terms of the downwash angle rather than the inflow velocity is that the downwash angle is a nondimensional parameter independent of operating speed. For the particular prototype described by Table 1 the calculated downwash angle is $4.4°$ while the inflow velocity varies from $0.9\,\mathrm{m/s}$ to $2.8\,\mathrm{m/s}$ at test speeds from $100\,\mathrm{rad/s}$ to $300\,\mathrm{rad/s}$.

$$\phi_{3/4} = \frac{a\sigma}{12}\left(\sqrt{1 + \frac{24\theta_0}{a\sigma}} - 1\right) \tag{21}$$

The evaluated integrals for the full moments about the hub, lag, and flap axes are given in Eqs. 22–24, now written in terms of the Lock number γ. The distinguishing feature of this result in comparison to [11] is the dependence on ω following from consideration of a non-constant hub velocity $\dot{\psi} = \Omega + \omega$.

$$
\begin{aligned}
M_{\psi_{aero}} = \frac{1}{8}\gamma I_\beta \Omega^2 \Big\{ &-\frac{c_{d_0}}{a} + \phi_{3/4}^2 - \theta\left(\phi_{3/4}\right) \\
&- \frac{\omega}{\Omega}\left(2\frac{c_{d_0}}{a} + \theta\phi_{3/4}\right) \\
&+ \frac{\dot{\zeta}}{\Omega}\left((2\frac{c_{d_0}}{a} + \theta\phi_{3/4})(1 - \frac{4}{3}e)\right) \\
&- \frac{\dot{\beta}}{\Omega}\left((\theta - 2\phi_{3/4})(1 - \frac{4}{3}e)\right)\Big\}
\end{aligned}
\tag{22}
$$

$$
\begin{aligned}
M_{\zeta_{aero}} = \frac{1}{8}\gamma I_\beta \Omega^2 \Big\{ &(\frac{c_{d_0}}{a} - \phi_{3/4}^2)(1 - \frac{4}{3}e) + \theta\left(\phi_{3/4}(1 - \frac{4}{3}e)\right) \\
&+ \frac{\omega}{\Omega}\left((2\frac{c_{d_0}}{a} + \theta\phi_{3/4})(1 - \frac{4}{3}e)\right) \\
&- \frac{\dot{\zeta}}{\Omega}\left((2\frac{c_{d_0}}{a} + \theta\phi_{3/4})(1 - \frac{8}{3}e + 2e^2)\right) \\
&+ \frac{\dot{\beta}}{\Omega}\left((\theta - 2\phi_{3/4})(1 - \frac{8}{3}e + 2e^2)\right)\Big\}
\end{aligned}
\tag{23}
$$

$$M_{\beta_{aero}} = \frac{1}{8}\gamma I_\beta \Omega^2 \Bigg\{ -(1+\frac{c_{d_0}}{a})\phi_{3/4}(1-\frac{4}{3}e) + \theta\left(1-\frac{4}{3}e\right)$$

$$+ \frac{\omega}{\Omega}\left((2\theta - (1+\frac{c_{d_0}}{a})\phi_{3/4})(1-\frac{4}{3}e)\right)$$

$$- \frac{\dot{\zeta}}{\Omega}\left((2\theta - (1+\frac{c_{d_0}}{a})\phi_{3/4})(1-\frac{8}{3}e+2e^2)\right)$$

$$- \frac{\dot{\beta}}{\Omega}\left((1+\frac{c_{d_0}}{a})(1-\frac{8}{3}e+2e^2)\right)\Bigg\}$$

(24)

The final generalized moment vector required for the overall equation of motion Eq. 6 is $N = \{-M_{\psi_{aero}}, -M_{\zeta_{aero}}, -M_{\beta_{aero}}\}$; incorporating moments about the hub, lag, and flap axes given in Eqs. 22–24. Near trim at speed Ω, this can be written affine in the perturbation angles x and rates $\dot{x}$ defined in Eq. 5. The dependence on lag angle is due only to enforcing the lag-pitch coupling constraint $\theta = \theta_0 + (\Delta\theta/\Delta\zeta)\tilde{\zeta}$. A positive value for $\Delta\theta/\Delta\zeta$ permits a rearward lag deflection to increase blade pitch and upward flapping moment, and a negative value for $\Delta\theta/\Delta\zeta$ has the opposite effect.

$$N = \frac{1}{8}\gamma I_\beta \Omega^2 \begin{bmatrix} (\theta_0\phi_{3/4} - \phi_{3/4}^2 + \frac{c_{d_0}}{a}) \\ -(\theta_0\phi_{3/4} - \phi_{3/4}^2 + \frac{c_{d_0}}{a})(1-\frac{4}{3}e) \\ -(\theta_0 - \phi_{3/4} - \frac{c_{d_0}}{a}\phi_{3/4})(1-\frac{4}{3}e) \end{bmatrix}$$

$$+ \frac{1}{8}\gamma I_\beta \Omega^2 \begin{bmatrix} (2\frac{c_{d_0}}{a}+\theta_0\phi_{3/4}) & -(2\frac{c_{d_0}}{a}+\theta_0\phi_{3/4})(1-\frac{4}{3}e) & (\theta_0-2\phi_{3/4})(1-\frac{4}{3}e) \\ -(2\frac{c_{d_0}}{a}+\theta_0\phi_{3/4})(1-\frac{4}{3}e) & (2\frac{c_{d_0}}{a}+\theta_0\phi_{3/4})(1-\frac{8}{3}e+2e^2) & -(\theta_0-2\phi_{3/4})(1-\frac{8}{3}e+2e^2) \\ -(2\theta_0-(1+\frac{c_{d_0}}{a})\phi_{3/4})(1-\frac{4}{3}e) & (2\theta_0-(1+\frac{c_{d_0}}{a})\phi_{3/4})(1-\frac{8}{3}e+2e^2) & (1+\frac{c_{d_0}}{a})(1-\frac{8}{3}e+2e^2) \end{bmatrix}\dot{x}$$

$$+ \frac{1}{8}\gamma I_\beta \Omega^2 \begin{bmatrix} \phi_{3/4} \\ -\phi_{3/4}(1-\frac{4}{3}e) \\ -(1-\frac{4}{3}e) \end{bmatrix}\begin{bmatrix} 0 & \frac{\Delta\theta}{\Delta\zeta} & 0 \end{bmatrix} x$$

(25)

C. Hinge Losses

Rotational friction in the physical flap hinge and skewed lag-pitch hinge cause energy losses which must be represented in the dynamical model. These effects are lumped into equivalent nondimensional linear damping coefficients c_β and c_ζ for flap and lag in the analysis. Instead of fitting these parameters from data, reasonable estimates are derived by an energy argument which highlights some expected scaling relations for these coefficients.

The pin joints are principally loaded by the outward centrifugal force F of the spinning blade which can be computed by integrating $\Omega^2 R \xi \, dm$ over the mass of the blade.

$$F = \frac{1}{2} mR(1+e)\Omega^2 = \frac{3}{2} I_\beta \Omega^2 \frac{1}{R} \frac{1+e}{(1-e)^2} \tag{26}$$

The physical flap hinge of Fig. 2 is modeled as a plain journal bearing or short shoe brake, for which the friction torque τ_{ξ_1} depends on the coefficient of friction μ_1 between the steel pin and plastic hole, the radius of the pin R_P, and the side load force F [15]. A nondimensional pin geometry parameter G_P is defined such that $R_P = G_P R$. The work done by friction torque τ_{ξ_1} integrated over one cycle of flap amplitude A_β is W_{ξ_1}.

$$\tau_{\xi_1} = \mu_1 G_P R F \tag{27}$$

$$W_{\xi_1} = 6 I_\beta \Omega^2 A_\beta \mu_1 G_P \frac{1+e}{(1-e)^2} \tag{28}$$

If instead, a linear damping model about the flap coordinate were considered, the flap hinge torque τ_β would be proportional to the velocity by nondimensional damping coefficient c_β and normalizing factor $I_\beta \Omega$. The integrated viscous work W_β over one cycle can be calculated based on the angular amplitude A_β and frequency Ω.

$$\tau_\beta = I_\beta \Omega c_\beta \dot{\beta} \tag{29}$$

$$W_\beta = \pi I_\beta \Omega^2 A_\beta^2 c_\beta \tag{30}$$

The energy equivalent nondimensional damping c_β is found by equating these two different expressions for the flap cycle work. It is seen to depend only on the ratiometric geometry of the propeller, the friction coefficient, and the nominal amplitude. In particular this coefficient is independent of absolute scale or operating speed.

$$c_\beta = \frac{6}{\pi} \frac{\mu_1 G_P}{A_\beta} \frac{1+e}{(1-e)^2} \tag{31}$$

The skewed lag-pitch hinge experiences a friction torque τ_{ξ_2} which is the sum of two terms. The first term is a plain bearing friction torque under a side load of $F\cos(\delta)$. In addition, a large axial load $F|\sin(\delta)|$ is carried by two plastic washers of radius R_D which slide against each other with material coefficient of friction μ_2. This contributes a second term to the friction torque about the

skew axis, which is modeled as the torque of a uniform pressure contact disk brake [15]. Once again a geometric parameter G_D for these disks is introduced such that $R_D = G_D R$. The friction work W_{ξ_2} of torque τ_{ξ_2} integrated over one cycle of lag amplitude A_ζ is computed, recognizing from the geometry of Fig. 2 that the skew hinge axis rotates with an amplitude $A_\zeta / \cos(\delta)$.

$$\tau_{\xi_2} = \mu_1 G_P R F \cos(\delta) + \frac{2}{3}\mu_2 G_D R F |\sin(\delta)| \tag{32}$$

$$W_{\xi_2} = 6I_\beta\Omega^2 A_\zeta \mu_1 G_P \frac{1+e}{(1-e)^2} + 4I_\beta\Omega^2 A_\zeta \mu_2 G_D \frac{1+e}{(1-e)^2}|\tan(\delta)| \tag{33}$$

As before, setting this friction work expression equal to a damping work expression allows an equivalent nondimensional damping coefficient c_ζ to be defined for the conventional lag coordinate in the dynamics.

$$c_\zeta = \frac{6}{\pi}\frac{1}{A_\zeta}\left(\mu_1 G_P + \frac{2}{3}\mu_2 G_D |\tan(\delta)|\right)\frac{1+e}{(1-e)^2} \tag{34}$$

The final contribution to the overall dynamics in Eq. 6, $\boldsymbol{\tau}_{hinge}$, is now written in terms of these damping coefficients and the coordinate velocities $\dot{\boldsymbol{x}} = (\omega, \dot{\zeta}, \dot{\beta})$.

$$\boldsymbol{\tau}_{hinge} = \begin{bmatrix} 0 & 0 & 0 \\ 0 & -I_\beta\Omega c_\zeta & 0 \\ 0 & 0 & -I_\beta\Omega c_\beta \end{bmatrix} \dot{\boldsymbol{x}} \tag{35}$$

The naive linear model requires choosing representative amplitudes A_ζ and A_β to determine coefficients c_ζ and c_β. Instead of making such an assumption, the equation of motion can be solved iteratively to determine A_ζ and A_β for a particular drive amplitude. This approach was used to determine the theory curves for comparison with the experimental data in Section V, and allows the model to predict the characteristic low amplitude nonlinearity in the gain response evident in Fig. 11.

D. Motor Equation And Speed Governor

The shaft torque required to overcome the rotor aerodynamic drag as well as excite the desired lag-pitch motion for cyclic control is generated by a single brushless electric motor. The motor torque Q obeys the basic DC motor model of Eq. 36. The applied terminal voltage V induces an electrical current i subject to the electrical motor constant K_e and electrical resistance R_{ohm}. The

torque Q is proportional to the current i less the no load current i_0.

$$Q = K_e(i - i_0)$$

$$i = \frac{1}{R_{ohm}}(V - K_e\dot{\psi}) \tag{36}$$

An average rotor speed Ω is maintained by employing a software defined proportional-integral (PI) control law with gains K_P and K_I. The applied voltage V is calculated according to Eq. 37 as the sum of three parts: the proportional control term, the integral control term, and an added sinusoidal signal $\tilde{V}$ used to excite the lag-pitch mode. During experiments, $\tilde{V}$ is computed as $\tilde{V} = A\cos\psi$ based on a desired voltage amplitude A and the instantaneous hub orientation ψ.

$$V = -K_P(\dot{\psi} - \Omega) - K_I \int (\dot{\psi} - \Omega)dt + \tilde{V} \tag{37}$$

The resulting motor torque is given by Eq. 38. The first two terms reflect the action of the proportional and integral control laws, while the remainder of the expression only depends on the physical motor properties.

$$Q = -\frac{K_P K_e}{R_{ohm}}(\dot{\psi} - \Omega) - \frac{K_I K_e}{R_{ohm}} \int (\dot{\psi} - \Omega)dt + \frac{K_e}{R_{ohm}}\tilde{V} - \frac{K_e^2}{R_{ohm}}\dot{\psi} - K_e i_0 \tag{38}$$

In steady operation with imposed $\tilde{V} = 0$ the integral control action ensures the rotor reaches a steady trim state with hub speed $\dot{\psi}$ equal to constant Ω and the motor torque Q taking a constant value Q_0. This trim condition is expressed in Eq. 39.

$$Q_0 = -\frac{K_I K_e}{R_{ohm}} \int (\dot{\psi} - \Omega)dt - \frac{K_e^2}{R_{ohm}}\Omega - K_e i_0 \tag{39}$$

The motor equation may be rewritten relative to this trim state in terms of perturbation variables $\tilde{Q} = Q - Q_0$ and $\omega = \dot{\psi} - \Omega$. In Eq. 40 the integral of ω is furthermore defined to be the (virtual) angle $\tilde{\psi}$ satisfying $\tilde{\psi} = \psi - \Omega t$.

$$\tilde{Q} = -(K_P + K_e)\frac{K_e}{R_{ohm}}\omega - K_I\frac{K_e}{R_{ohm}}\tilde{\psi} + \frac{K_e}{R_{ohm}}\tilde{V} \tag{40}$$

Equation 40 suggests the combined effects of the motor dynamics and speed governor are to act as a damping term on velocity ω with coefficient c_m and stiffness term on the (virtual) angle $\tilde{\psi}$ with coefficient k_m. The vector of joint torques due to the motor $\boldsymbol{\tau}_{motor}$ required by Eq. 6 can finally be

written in vector form in terms of the perturbation variables $\boldsymbol{x}$, $\dot{\boldsymbol{x}}$ defined in Eq. 5 and the imposed sinusoidal input $\tilde{V}$.

$$c_m = (K_P + K_e)\frac{K_e}{R_{ohm}} \qquad k_m = K_I \frac{K_e}{R_{ohm}} \tag{41}$$

$$\boldsymbol{\tau}_{motor} = \begin{bmatrix} Q_0 \\ 0 \\ 0 \end{bmatrix} + \begin{bmatrix} -k_m & 0 & 0 \\ 0 & 0 & 0 \\ 0 & 0 & 0 \end{bmatrix} \boldsymbol{x} + \begin{bmatrix} -c_m & 0 & 0 \\ 0 & 0 & 0 \\ 0 & 0 & 0 \end{bmatrix} \dot{\boldsymbol{x}} + \begin{bmatrix} \frac{K_e}{R_{ohm}} \\ 0 \\ 0 \end{bmatrix} \tilde{V} \tag{42}$$

E. Equilibrium

Suppose that a constant applied motor torque Q_0 yields a steady trim state where the propeller spins with velocity Ω. The steady coordinate configuration is $\boldsymbol{q}_0 = (\Omega t, \zeta_0, \beta_0)$ and the velocities are $\dot{\boldsymbol{q}}_0 = (\Omega, 0, 0)$ for constant Ω. Further assume that in this state the residual internal static friction torques at the joints are zero. This assumed solution can be inserted into the equation of motion (Eq. 6) to solve for the unknown angles ζ_0 and β_0 and unknown drive torque Q_0. Under these conditions the steady Coriolis term $\boldsymbol{C}_0$, aerodynamic forces $\boldsymbol{N}_0$, and applied motor torque Q_0 obey the equilibrium expressed in Eq. 43.

$$\boldsymbol{C}_0 + \boldsymbol{N}_0 = \begin{bmatrix} Q_0/N_b \\ 0 \\ 0 \end{bmatrix} \tag{43}$$

The Coriolis term $\boldsymbol{C}_0$ was given previously in Eq. 10. The aerodynamic force $\boldsymbol{N}_0$ comes from the constant term in Eq. 25. The resulting equilibrium is now given by Eq. 44 where θ_0 is the collective blade pitch and $\phi_{3/4}$ is the downwash angle given by Eq. 21.

$$I_\beta \Omega^2 \begin{bmatrix} 0 \\ \frac{3e}{2(1-e)}\zeta_0 \\ \frac{2+e}{2(1-e)}\beta_0 \end{bmatrix} + \frac{1}{8}\gamma I_\beta \Omega^2 \begin{bmatrix} (\theta_0\phi_{3/4} - \phi_{3/4}^2 + \frac{c_{d_0}}{a}) \\ -(\theta_0\phi_{3/4} - \phi_{3/4}^2 + \frac{c_{d_0}}{a})(1 - \frac{4}{3}e) \\ -(\theta_0 - \phi_{3/4} - \frac{c_{d_0}}{a}\phi_{3/4})(1 - \frac{4}{3}e) \end{bmatrix} = \begin{bmatrix} Q_0/N_b \\ 0 \\ 0 \end{bmatrix} \tag{44}$$

The trim drive torque given by Eq. 45 is obtained immediately from the first row. The corresponding shaft torque coefficient C_Q is computed in Eq. 46 from its definition after substituting in the disc solidity σ [14]. This trim value for the shaft torque coefficient provides context for the

magnitude of the torque modulation used for cyclic control in the experiments.

$$Q_0 = \frac{1}{8}\gamma I_\beta \Omega^2 N_b(\theta_0\phi_{3/4} - \phi_{3/4}^2 + \frac{c_{d_0}}{a}) \tag{45}$$

$$C_Q = \frac{1}{8}a\sigma(\theta_0\phi_{3/4} - \phi_{3/4}^2 + \frac{c_{d_0}}{a}) \tag{46}$$

The lag and flap angles are found by solving the second and third row equations.

$$\zeta_0 = \frac{(1 - \frac{4}{3}e)(1 - e)}{12e}\gamma(\theta_0\phi_{3/4} - \phi_{3/4}^2 + \frac{c_{d_0}}{a})$$
$$\beta_0 = \frac{(1 - \frac{4}{3}e)(1 - e)}{8(1 + \frac{1}{2}e)}\gamma(\theta_0 - \phi_{3/4} - \frac{c_{d_0}}{a}\phi_{3/4}) \tag{47}$$

F.   Linearized System Equations

The governing equations for small variations in the hub, lag, and flap motion with respect to equilibrium are found by substituting into Eq. 6 from Eq. 7-9, 25, 35, and 42 and discarding the constant terms associated with trim. This results in a linear system of equations in the state vector $\boldsymbol{x} = \{\tilde{\psi}, \tilde{\zeta}, \tilde{\beta}\}$ with a single input which is the voltage excitation $\tilde{V}$ imposed to drive the cyclic response. We are primarily interested in the 1/rev system response because in practice the excitation is a function of the hub rotation, $\tilde{V} = A\cos\psi$ with some amplitude A. As a result it is convenient to introduce a nondimensional time $\hat{t}$ such that $\hat{t} = \Omega t$. Coordinate derivatives are rewritten nondimensionally where now $\boldsymbol{x}'$ and $\boldsymbol{x}''$ are derivatives of coordinates $\boldsymbol{x}$ with respect to nondimensional time $\hat{t}$.

$$\boldsymbol{x} = \begin{bmatrix} \tilde{\psi} & \tilde{\zeta} & \tilde{\beta} \end{bmatrix}$$
$$\boldsymbol{x}' = \begin{bmatrix} \frac{\omega}{\Omega} & \frac{\dot{\zeta}}{\Omega} & \frac{\dot{\beta}}{\Omega} \end{bmatrix}$$
$$\boldsymbol{x}'' = \begin{bmatrix} \frac{\dot{\omega}}{\Omega^2} & \frac{\ddot{\zeta}}{\Omega^2} & \frac{\ddot{\beta}}{\Omega^2} \end{bmatrix} \tag{48}$$

We similarly wish to nondimensionalize the input voltage excitation $\tilde{V}$ in a physically meaningful way in order to permit comparisons between systems with very different motor electrical characteristics. We choose to define a nondimensional scaled input u which is proportional to $\tilde{V}$, defined in Eq. 49. The scale factor is suggested by observing that, under the motor model of Eq. 36, the motor torque rises proportional to an instantaneous increment in voltage by a constant of K_e/R_{ohm}. This

torque can then be normalized by a factor of $\rho\pi R^5\Omega^2$, or equivalently $N_b I_\beta \gamma \Omega^2/(a\sigma)$, in similarity to how the rotor torque coefficient C_Q is conventionally defined [14]. The input u is the input to the full rotor system, so it is divided by N_b in the single blade equation.

$$u = \frac{1}{\rho\pi R^5\Omega^2}\frac{K_e}{R_{ohm}}\tilde{V} = \frac{a\sigma}{N_b I_\beta \gamma \Omega^2}\frac{K_e}{R_{ohm}}\tilde{V} \tag{49}$$

The final nondimensional equation of motion for the half propeller is obtained after dividing through by Ω^2 as well as the flap inertia I_β to obtain Eq. 50. The coefficient matrices owing to aerodynamic terms have been held separate from those describing inertial, motor, and friction dynamics to highlight their contributions to the overall model. Given this linear state space model, the cyclic hub speed, lag, and flap response are found directly by evaluating the associated transfer functions from the input u at frequency 1 (once-per-revolution excitation).

$$
\begin{bmatrix}
1 + X_{I_h} + \frac{3e}{(1-e)^2} & -1 - \frac{3e}{2(1-e)} & 0 \\
-1 - \frac{3e}{2(1-e)} & 1 & 0 \\
0 & 0 & 1
\end{bmatrix}\boldsymbol{x}'' +
\left(
\begin{bmatrix}
\frac{c_m}{\Omega I_\beta}/N_b & -\frac{3e}{1-e}\zeta_0 & -(2+\frac{3e}{1-e})\beta_0 \\
\frac{3e}{1-e}\zeta_0 & c_\zeta & 2\beta_0 \\
(2+\frac{3e}{1-e})\beta_0 & -2\beta_0 & c_\beta
\end{bmatrix}
\right.
$$

$$
\left. + \frac{1}{8}\gamma
\begin{bmatrix}
(2\frac{c_{d0}}{a}+\theta_0\phi_{3/4}) & -(2\frac{c_{d0}}{a}+\theta_0\phi_{3/4})(1-\frac{4}{3}e) & (\theta_0-2\phi_{3/4})(1-\frac{4}{3}e) \\
-(2\frac{c_{d0}}{a}+\theta_0\phi_{3/4})(1-\frac{4}{3}e) & (2\frac{c_{d0}}{a}+\theta_0\phi_{3/4})(1-\frac{8}{3}e+2e^2) & -(\theta_0-2\phi_{3/4})(1-\frac{8}{3}e+2e^2) \\
-(2\theta_0-(1+\frac{c_{d0}}{a})\phi_{3/4})(1-\frac{4}{3}e) & (2\theta_0-(1+\frac{c_{d0}}{a})\phi_{3/4})(1-\frac{8}{3}e+2e^2) & (1+\frac{c_{d0}}{a})(1-\frac{8}{3}e+2e^2)
\end{bmatrix}
\right)\boldsymbol{x}'
$$

$$
+ \left(
\begin{bmatrix}
\frac{k_m}{\Omega^2 I_\beta}/N_b & 0 & 0 \\
0 & \frac{3e}{2(1-e)} & 0 \\
0 & 0 & 1+\frac{3e}{2(1-e)}
\end{bmatrix}
+ \frac{1}{8}\gamma
\begin{bmatrix}
\phi_{3/4} \\
-\phi_{3/4}(1-\frac{4}{3}e) \\
-(1-\frac{4}{3}e)
\end{bmatrix}
\begin{bmatrix}
0 & \frac{\Delta\theta}{\Delta\zeta} & 0
\end{bmatrix}
\right)\boldsymbol{x} =
\begin{bmatrix}
\frac{\gamma}{a\sigma} \\
0 \\
0
\end{bmatrix} u \tag{50}
$$

The key interest for aircraft controls design will be the amplitude and phase relation between the input u and the ensuing cyclic pitch variation or flapping motion. In the case of small collective pitch θ_0 and small trim angles ζ_0 and β_0 the sparse dominant terms in Eq. 50 can be qualitatively interpreted as a cascaded response to the input u. Recalling that the state vector is ordered $\boldsymbol{x} = \{\tilde{\psi}, \tilde{\zeta}, \tilde{\beta}\}$, the voltage modulation described by u is seen to only contribute directly to the hub acceleration. This hub acceleration is coupled into lag accelerations primarily through the inertia matrix. Lag deflections induce pitch changes by the geometric constant $\Delta\theta/\Delta\zeta$, and the resulting aerodynamic forces drive the flap motion.

The nondimensional governing equations are almost entirely independent of absolute scale in terms of either physical extent (R, I_β, m, etc.) or operating speed (Ω). The only exception are the groupings $c_m/(\Omega I_\beta)$ and $k_m/(\Omega^2 I_\beta)$ related to the motor dynamics. Since the effective motor stiffness and damping coefficients c_m and k_m are determined by choice of software speed control gains it is straightforward to conduct experiments at varied scales and speeds with identical governing equations.

IV.   Prototype Construction

A 32 cm diameter propeller embodying the kinematics of Section II was constructed. In combination with a commercial motor and custom electronic motor drive, the device allows controlled experiments of the cyclic system during which torque, speed, blade lag angle, and blade flap angle can be measured. The propeller shown in Fig. 4 is constructed from 3D printed plastic parts joined by simple stainless steel pins. The visible plastic screws serve only to retain the pins in place. The blade is an commercial 11% thick, symmetric airfoil bonded into the custom blade grip. Two polytetrafluoroethylene (PTFE) plastic washers in the lag hinge serve as thrust bearings to reduce the hinge friction under centrifugal loading.

Critical rotor parameters for model calculations are summarized in Table 1. The eccentricity e of the hinge location was chosen to be 0.076 which was the smallest practical value given the construction methods. A representative lift curve slope of $0.1\,/°$ and drag coefficient of 0.06 are used, though studies of similar NACA 0012 airfoils [16] caution that these numbers are uncertain at the varying low Reynolds numbers ($Re < 6.1 \times 10^4$) of these experiments. The characteristic friction coefficients of the plastic-plastic sliding contact and the silicone-lubricated steel-plastic interfaces were estimated in separate tilted-plane tests.

The motor and brushless motor controller drive the propeller rotation and are responsible for applying the once-per-revolution modulation of torque to excite the cyclic mode. The motor is a common brushless motor with a rotating shaft exposed at both ends. The motor orientation is directly measured by a contactless 4096-count magnetic rotary encoder mounted beneath the motor on the controller circuit board, shown in Fig. 4. This sensor observes the rotation of a diametrically polarized magnet bonded to the shaft end. These angle measurements are used to update the motor

Table 1 Propeller properties.

parameter	symbol	value
tip radius	R	159 mm
number blades	N_b	2
hinge eccentricity	e	0.076
washer disk radius	R_D	1.98 mm
hinge pin radius	R_P	0.52 mm
blade mass	m	5.40 g
hub rotational inertia	-	5.1×10^{-7} kg m^2
blade chord	c	19.3 mm
blade pitch	θ_0	9°
section drag coef	c_{d_0}	0.06
section lift curve slope	a	0.1 /°
friction coef steel-plastic	μ_1	0.20
friction coef plastic-plastic	μ_2	0.07
air density	ρ	1.2 kg/m^3
downwash angle	$\phi_{3/4}$	4.4°
flap inertia	I_β	3.9×10^{-5} kg m^2
Lock number	γ	2.18

winding commutation at 40 kHz and update the speed controller at 2 kHz. In addition, this direct measurement of the hub rotation is used to calculate the modulation voltage $\tilde{V}$ in order to ensure the phase and frequency of modulation remain synchronous with the hub rotation. The critical parameters for the electronic drive system are summarized in Table 2. The motor inertia, emf constant, and combined effective resistance of the motor and driver circuitry are fit values based on separate frequency response testing of the bare motor without an attached propeller.

During experiments the rotor is supported on a vertical pylon to hold it out of ground effect. Thrust forces and reaction torques are measured by a small six-axis load cell atop the supporting pylon. The drive module of Fig. 4 containing the power electronics and motor is mounted directly to the load cell. The propeller is mounted to the rotating face of the motor by two screws to ensure
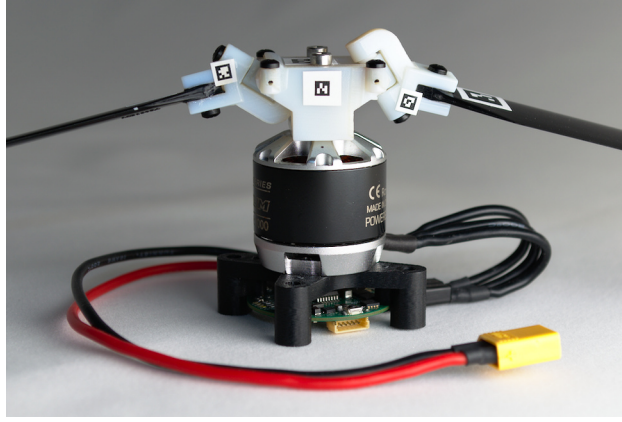
Fig. 4 Power electronics, motor, and articulated hub for a 318 mm diameter cyclic rotor.

Table 2 Motor properties and control gains for 200 rad/s test speed.

parameter	symbol	value
emf constant	K_e	0.00954 V/(rad/s) or N m/A
resistance	R_{ohm}	0.305 ohms
motor rotational inertia	-	3.26×10^{-6} kg m^2
proportional speed gain	K_P	0.03 V/(rad/s)
integral speed gain	K_I	0.03 V/rad

the propeller does not slip relative to the motor during testing.

V. Experiments

Experiments were conducted at mean rotor speeds of $100\,\mathrm{rad/s}$, $200\,\mathrm{rad/s}$, and $300\,\mathrm{rad/s}$ to determine the sensitivity of the cyclic response to drive amplitude inputs. During low speed and high speed tests, the nominal speed governor gains of Table 2 are scaled such that the nondimensional motor coefficients of Eq. 41 obtain identical equations of motion in Eq. 50. As a result, measured amplitudes and phase shifts for the torque, hub speed, lag angle, and flap angle response at different test speeds should all fall on single curves from the theory when properly scaled.

At each test speed, a range of amplitudes A for the additive, phase locked excitation voltage $\tilde{V} = A\cos\psi$ are applied and the steady cyclic responses measured. Torque values are derived from the load cell, and hub speed and position measurements are reported by the motor controller.

Lag angles are derived from top-down high speed video imagery, and flap angles are derived from side-view strobe photography. Synchronization of these sources is achieved by having the motor controller emit a digital index signal read by the load cell DAQ as well as a visible indicator for the high speed video.

The equation of motion developed for the half-propeller in Eq. 50 takes advantage of approximate symmetry to describe the dynamics of a single blade instead of explicitly modeling two blades. To practice cyclic control, one of the blades is mounted with a positive lag-pitch coefficient $\Delta\theta/\Delta\zeta$ and the other is mounted with a negative lag-pitch coefficient, as shown in Fig. 2. Model predictions for both the positive and negative case are plotted against the measured data – the difference is only notable in the case of flap, where the purpose of the cyclic system is to ensure the positive and negative blades remain $180°$ out of phase with each other. The model state space could be extended to explicitly encompass the full system with two independent dissimilar blades, but the simplified model used here exposes the fundamental physics being exploited and makes satisfactory numerical predictions.

A.   Motor Torque

The amplitude and phase of the first harmonic of the motor reaction torques are plotted in Figs. 5-6 and compared to model predictions for a range of drive voltage amplitudes at three different operating speeds. The motor torques are shown normalized by $\rho\pi R^5\Omega^2$ so that they may be put in the context of the propeller torque coefficient $C_Q = 0.92 \times 10^{-3}$ as calculated from Eq. 46. The normalized drive amplitudes u are calculated at each test condition from the definition in Eq. 49, so that u grows in direct proportion to $\tilde{V}$ for tests conducted at identical average speeds. The input u may be thought of as one of the three terms in Eq. 40 which sum to the shaft torque, so it is not surprising that in Fig. 5 the normalized torque amplitude closely follows u. Predictions of the torque response amplitude are accurate, but the torque lags the 1/rev modulation in u by up to $15°$ less than predicted by the model.

Modulating torque incurs a reduction in energy efficiency because the instantaneous power lost to resistance heating inside the motor grows as the square of the torque. This loss can be offset by saved vehicle weight as in the specific example of [10], but it may be advantageous to optimize
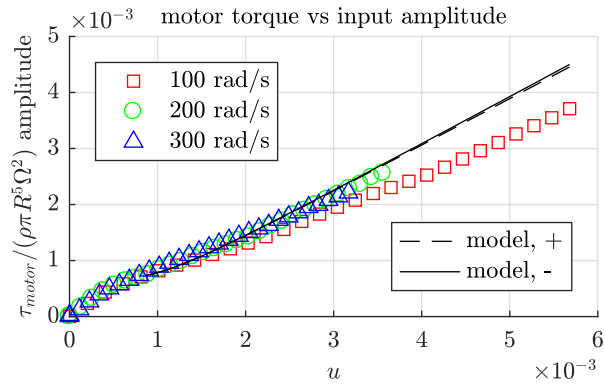
25

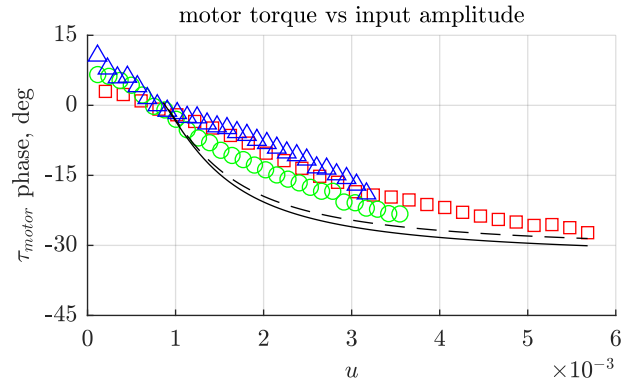**Fig. 5 Motor torque response amplitude at three test speeds.**

Fig. 6 Motor torque response phase at three test speeds.

rotors to require less torque modulation for operation.

B. Hub Speed Response

Variations in the hub speed are easily measured by the motor controller and provide an indicator of the magnitude of the excited lag-pitch-flap response. In these tests the rotor reference speed Ω is fixed, an applied additive voltage amplitude is set, and the cyclic response is obtained. The lag and flap response is obtained rapidly, and we wait several seconds for any transient response of the weak integral speed control law to settle completely before beginning measurements. Speed and position data are sampled for five seconds, representing more than a hundred revolutions of the propeller. The scatter plot of instantaneous hub speed vs position in Fig. 7 compounds one second of continuous data, demonstrating that the hub speed variation is phase locked with the rotation and extremely consistent from one revolution to the next. The response can be summarized by the

26
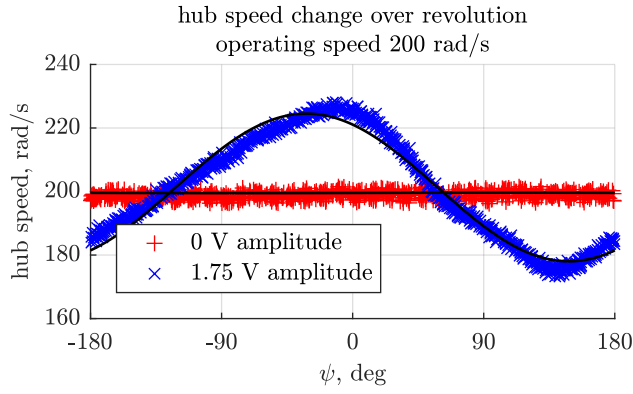
Fig. 7 Phase locked hub speed change over one revolution at 200 rad/s.
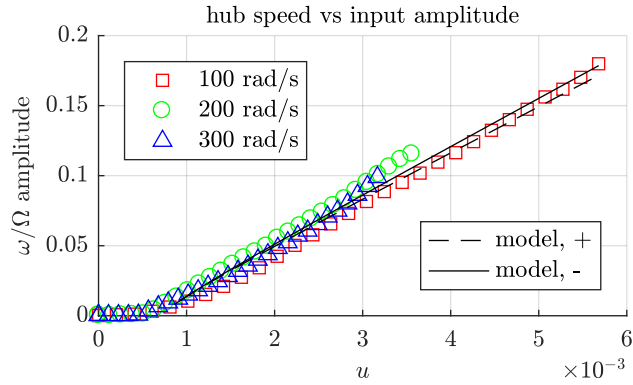
Fig. 8 Hub speed variation ω response amplitude at three test speeds Ω.

amplitude and phase of the first harmonic fit, also shown.

The hub speed variation ω amplitude and phase are summarized in Figs. 8-9 for a range of drive amplitudes as well as mean operating speeds Ω. For very low drive amplitudes the lag hinges are bound by static friction. In this operating state instead of the hub and blade being joined by a mobile hinge they act effectively as one large inertial mass, the multi-body model is no longer appropriate, and very little hub speed variation can be observed. After a critical drive amplitude, the hinges free and the speed variation begins to grow with the applied voltage modulation. The iterative approach described in Section III C for simultaneously solving the equation of motion and the amplitude parameters needed by the hinge damping model does a good job capturing this important nonlinearity in amplitude response, but the phase predictions are less accurate.

27
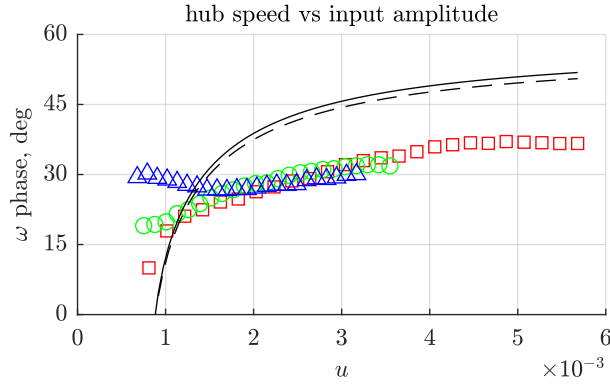
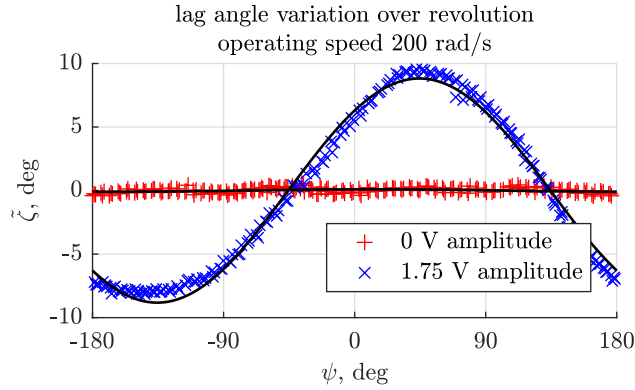**Fig. 9 Hub speed response phase at three test speeds.**

Fig. 10 Phase locked lag angle change over one revolution at 200 rad/s.

C. Lag Response

The lag response directly reveals the obtained cyclic pitch variation because the hinge geometry couples the lag and pitch angles. Blade lag angles for the positive coupling blade and negative coupling blade are determined by tracking AprilTag fiducial markers [17] attached to the tops of each blade root and the hub. Figure 10 collects measured lag angles for the positive coupling blade at different stations of the hub rotation over many operational cycles at 200 rad/s, both with and without an excitation voltage. The first harmonic fit to the data is shown alongside the measurements. For this particular prototype the geometric lag pitch couplings $\Delta\theta/\Delta\zeta$ were -1 and +1, so the lag amplitude shown in Fig. 10 reflects the amount of cyclic pitch variation obtained. The measured lag or pitch angles are well described by their first harmonic, which means that the pitch changes over a revolution are very similar to those a traditional swashplate system would prescribe.

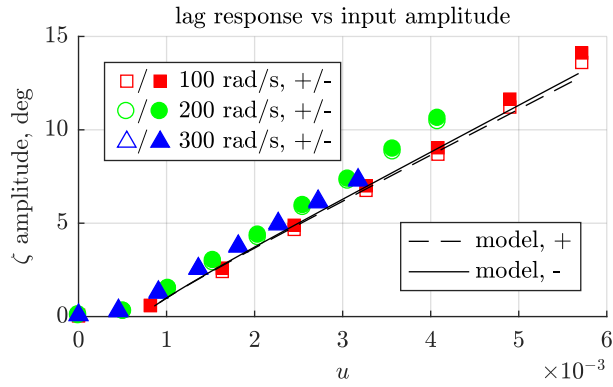The lag response amplitude and phase are tabulated over a range of operating speeds and drive

28

Fig. 11 Lag angle response amplitude for positive and negative lag-pitch blades.
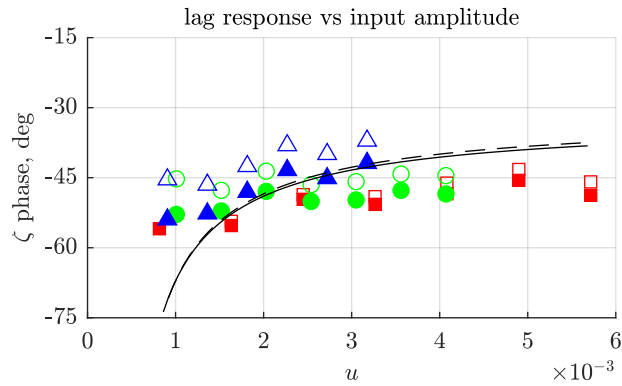

Fig. 12 Lag angle response phase for positive and negative lag-pitch blades.

amplitudes in Figs. 11-12 for both the positive coupled and negative coupled blades. The model accurately predicts the amplitude of the lag-pitch response, and therefore the degree of cyclic pitch control achieved. The minimum drive amplitude in u needed to excite a lag response corresponds with the knee in the hub speed response of Fig. 8, and both features indicate the threshold for breaking static friction in the hinge. Below this drive amplitude the hinges are friction bound, the model does not apply, and the phase of a zero amplitude response is not meaningful. The measured phase of the lag response is in agreement with the model for large drive amplitudes. However, at small amplitudes of motion the equivalent damping model introduced in Section III C may not accurately capture the more complex behavior of both static and dynamic friction. The sensitivity of cyclic pitch to cyclic voltage input shown by Figs. 11-12 is the effect exploited to initiate aircraft maneuvers by approximating cyclic pitch commands.
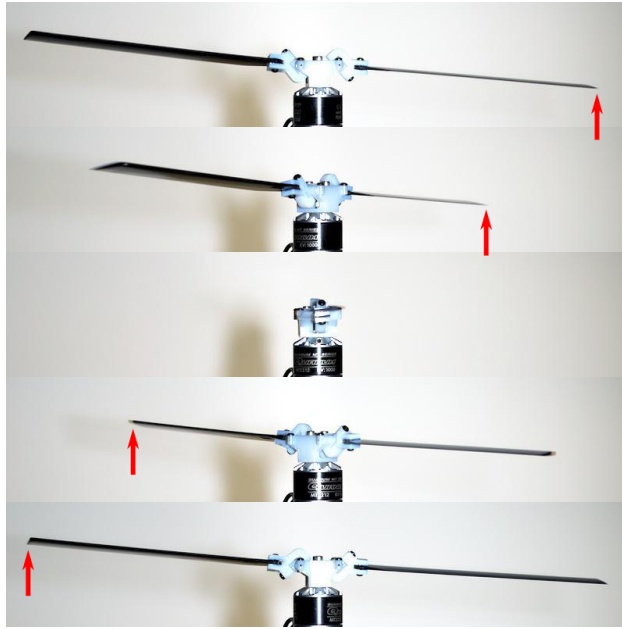
29

Fig. 13 Gross cyclic blade flap visible over one half revolution.

D. Flap Response

The ultimate objective of the cyclic system is to drive a coherent blade flapping response as a facsimile of conventional cyclic controls. Gross changes in the tip path plane are readily observed during testing. Figure 13 illustrates one half revolution of the propeller with a series of stroboscopic images showing the blade flap motion. Previous experiments with a similar rotor but lacking a flap hinge qualitatively displayed blade bending and higher harmonics in the blade tip flapping motions when observed in high speed video [9]. With the addition of a flap hinge, the flap motion is now concentrated at the hinge and the modeling assumption of rigid blades is appropriate. At the same time, the flap response now takes on the simple once-per-revolution character of a conventional articulated blade responding to cyclic pitch variations.

The degree of flapping is measured by tracking the orientation of fiducial markers on the front of the hub and blade grips in strobe photographs of the blade at different stations of the rotation. It is assumed that the flapping motion of the blade grips is representative of that of the blade as a whole – this assumption of rigidity is qualitatively supported by Fig. 13. Instead of physically rotating the test setup, the electronic modulation phase was rotated for each image. Figure 14 shows the flap angle response for the positive coupled blade through one revolution at an operating speed of
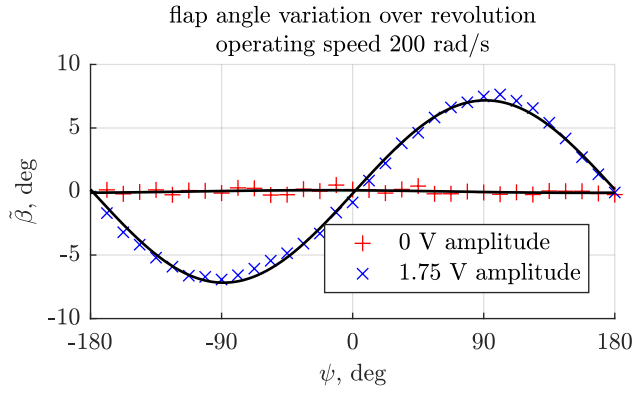
Fig. 14 Phase locked flap angle change over one revolution at 200 rad/s.

200 rad/s along with first harmonic fits to the measurements. As expected, the blade does not flap when no excitation voltage is applied. When a voltage amplitude of 1.75 V is applied, a smooth, first harmonic cyclic flapping response is obtained.

The flapping response phase and amplitude for both the positive and negative coupled blades are tabulated in Figs. 15-16 at a range of operating speeds and drive amplitudes. The positive and negative blades flap with approximately the same amplitude, but are approximately $180°$ out of phase with each other as required for a coherent tilting of the tip path plane as illustrated in the photographs of Fig. 13.

The model overestimates the flapping amplitudes by as much as a factor of two in spite of fairly accurate predictions for the blade pitch changes that aerodynamically drive that response. A likely reason for the disagreement is that a fixed radial inflow distribution was assumed when deriving aerodynamic forces on the blades, but in practice the downwash is not rotationally symmetric during heavy cyclic operation. This effects a reduction in obtained aerodynamic loads which is often approximated by a lift deficiency function with typical values near 0.5 for moment changes near hover [18]. Incorporating this effect into the model is expected to reduce the predicted aerodynamic loads and bring the predicted flapping response more in line with measurements.

VI.   Flight Applications and Future Work

The preceding experimental results and analytic modeling form a foundation for understanding the design and operation of the isolated rotor system near hover. Flight applications invite further
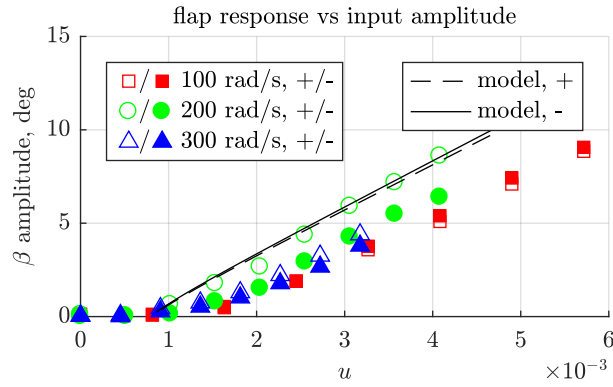
Fig. 15 Flap angle response amplitude for positive and negative lag-pitch blades.
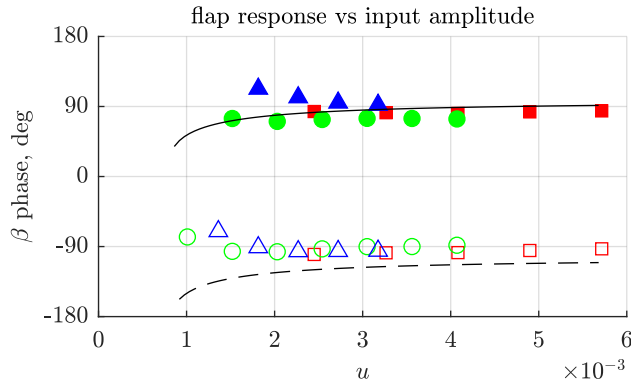

Fig. 16 Flap angle response phase for positive and negative lag-pitch blades.

questions regarding aircraft control integration, dynamic stability of the rotor in forward flight, and applicability to large manned aircraft, all of which are interesting directions for future work.

As with other fixed collective helicopters, thrust can be controlled by governing the average rotor head speed and complementary cyclic blade pitch changes do not significantly affect thrust. In addition, thrust is unaffected in an average sense over one revolution due to the new intentional cyclic variations in the hub speed and lag hinge speed. The available thrust bandwidth, however, will be limited by the fact that the rotor has been designed for a cyclic response to torque modulation at 1/rev. As a result, the dynamic response to changes in the reference speed Ω should be considered when selecting control gains K_P and K_I.

In future work the present model will permit a parametric stability analysis which may be verified experimentally. This study will need to consider both parameters of conventional interest such as the coupling $\Delta\theta/\Delta\zeta$ and collective pitch θ_0 as well as motor control parameters and the hub

32

inertia in order to identify forbidden regions of the design parameter space. The near hover model described by Eq. 50 covers only part of a practical aircraft's flight envelope. Forward flight also will induce 1/rev lead-lag motions of the blades. Extending the model to capture the forward flight condition would allow for stability and control analysis at high advance ratios, where previous flight tests have only been conducted at advance ratios of no more than 0.03 [10]. Similarly, the inclusion of aircraft angular velocity effects as well as the derivation of hub reaction forces and moments will give additional insight into the more dynamic maneuvers expected of micro air vehicles.

The equations of motion have no explicit dependence on scale, however, there are additional practical considerations for applying this technique in large aircraft. The shaft torque must be modulated at the rotor frequency. This is readily achieved by the electric motors employed in unmanned rotorcraft up to 1 m in diameter. Currently, larger manned rotorcraft rarely use electric motors. Reciprocating piston engines may also be capable of this modulation, as their combustion cycle frequency is much faster than the rotor speed. However, the turboshaft engines used in large manned helicopters will not commonly have the required control bandwidth. In manned aircraft the advantageous mechanical simplicity of this design over conventional swashplate systems may be offset by the need for exotic power plants or the need for redundant safety systems in case of power failure.

VII.   Conclusion

This work demonstrates that a specialized articulated rotor can approximate conventional cyclic blade pitch control simply by modulating the torque applied to the rotor hub once-per-revolution to excite a phase-locked lag-pitch response. We show that the addition of an explicit flap hinge to a skewed lag-pitch hinge permits a smooth harmonic flapping response. This improvement may enable a flight vehicle to exhibit reduced vibrations and a more conventional flapping tip path plane response to cyclic control than has been demonstrated in earlier work.

A linearized nondimensional equation of motion which explicitly models hub accelerations was developed based upon approximate kinematics, and experiments confirm that this model is descriptive over a range of operating speeds and control amplitudes. A minimum cyclic pitch authority of $\pm 7°$ was achieved at all test speeds and was accurately predicted by theory.

Future unmanned aerial vehicles employing this control effector may obtain the benefits of cyclic pitch control without the burdens associated with mechanical swashplate systems. New small, lightweight, and cost effective vehicles could be enabled by eliminating the need for swashplate actuators, servomotor or otherwise. At the same time, aircraft will benefit from avoiding conventional swashplate linkage and ball joint systems with their associated assembly and maintenance challenges.

VIII.   References

[1] Schafroth, D., Bermes, C., Bouabdallah, S., and Siegwart, R., "Micro Helicopter Steering: Review and Design for the muFly Project," *2008 IEEE/ASME International Conference on Mechatronic and Embedded Systems and Applications (MESA)*, Beijing, Oct. 2008, pp. 216–221. doi: 10.1109/MESA.2008.4735700.

[2] Cutler, M., Ure, N. K., Michini, B., and How, J. P., "Comparison of Fixed and Variable Pitch Actuators for Agile Quadrotors," *AIAA Guidance, Navigation, and Control Conference (GNC)*, AIAA 2011-6406, Portland, OR, 2011. doi:10.2514/6.2011-6406.

[3] Kim, S. K. and Tilbury, D. M., "Mathematical Modeling and Experimental Identification of an Unmanned Helicopter Robot with Flybar Dynamics," *Journal of Robotic Systems*, Vol. 21, No. 3, March 2004, pp. 95–116. doi:10.1002/rob.20002.

[4] Dadkhah, N. and Mettler, B., "System Identification Modeling and Flight Characteristics Analysis of Miniature Coaxial Helicopter," *Journal of the American Helicopter Society*, Vol. 59, No. 4, Oct. 2014, pp. 1–16. doi:10.4050/JAHS.59.042011.

[5] Schafroth, D., Bouabdallah, S., Bermes, C., and Siegwart, R., "From the Test Benches to the First Prototype of the muFly Micro Helicopter," *Journal of Intelligent and Robotic Systems*, Vol. 54, No. 1-3, March 2009, pp. 245–260. doi:10.1007/s10846-008-9264-z.

[6] George, S. and Samuel, P., "On the Design and Development of a Coaxial Nano Rotorcraft," *50th AIAA Aerospace Sciences Meeting*, 2012-0585, American Institute of Aeronautics and Astronautics, Nashville,

TN, Jan. 2012. doi:10.2514/6.2012-585.

[7] Fujihira, Y., Sasaki, R., and Ando, M., "Propeller Blade Tip Path Plane Inclining Device," US5259729 A, Nov. 1993.

[8] Reich, S., "Drehflügler, Rotorsystem Und Steuerung," WO2005087587 A1, Sept. 2005.

[9] Paulos, J. and Yim, M., "An Underactuated Propeller for Attitude Control in Micro Air Vehicles," *2013 IEEE/RSJ International Conference on Intelligent Robots and Systems (IROS)*, Tokyo, Nov. 2013, pp. 1374–1379. doi:10.1109/IROS.2013.6696528.

[10] Paulos, J. and Yim, M., "Flight Performance of a Swashplateless Micro Air Vehicle," *2015 IEEE International Conference on Robotics and Automation (ICRA)*, Seattle, WA, May 2015, pp. 5284–5289. doi:10.1109/ICRA.2015.7139936.

[11] Bousman, W. G., "The Effects of Structural Flap-Lag and Pitch-Lag Coupling on Soft Inplane Hingeless Rotor Stability in Hover," Tech. Rep. TP-3002, NASA, May 1990.

[12] Ormiston, R. A. and Hodges, D. H., "Linear Flap-Lag Dynamics of Hingeless Helicopter Rotor Blades in Hover," *Journal of the American Helicopter Society*, Vol. 17, No. 2, April 1972, pp. 2–14. doi: 10.4050/JAHS.17.2.

[13] Murray, R. M., Li, Z., and Sastry, S. S., *A Mathematical Introduction to Robotic Manipulation*, CRC Press, Boca Raton, 1994, pp. 171, 176.

[14] Leishman, G. J., *Principles of Helicopter Aerodynamics*, Cambridge University Press, Cambridge, 2nd ed., 2006, pp. 67, 127.

[15] Orthwein, W. C., *Clutches and Brakes: Design and Selection*, Marcel Dekker, New York, 2nd ed., Feb. 2004, pp. 37, 98.

[16] Kim, D.-H., Chang, J.-W., and Chung, J., "Low-Reynolds-Number Effect on Aerodynamic Characteristics of a NACA 0012 Airfoil," *Journal of Aircraft*, Vol. 48, No. 4, 2011, pp. 1212–1215. doi: 10.2514/1.C031223.

[17] Olson, E., "AprilTag: A Robust and Flexible Visual Fiducial System," *2011 IEEE International Conference on Robotics and Automation (ICRA)*, Shanghai, May 2011, pp. 3400–3407. doi: 10.1109/ICRA.2011.5979561.

[18] Johnson, W., *Helicopter Theory*, Dover Publications, New York, revised ed., 1994, p. 526.